

Demonstration of real-time depth-resolved Shack–Hartmann measurements

Jingyu Wang* and Adrian Gh. Podoleanu

Applied Optics Group, School of Physical Sciences, University of Kent, Canterbury, CT2 7NH, UK

*Corresponding author: j.y.wang@kent.ac.uk

Received September 14, 2012; revised October 18, 2012; accepted October 21, 2012;

posted October 22, 2012 (Doc. ID 176222); published November 22, 2012

Shack–Hartmann wavefront sensors (SH-WFS) have little sensitivity in depth and hence are unsuitable for microscopy and are limited for retinal imaging. We demonstrate the first direct Shack–Hartmann measurement of wavefront originating from a multiple-layer target, in the presence of significant stray reflections that render a standard SH-WFS inoperable. A coherence-gate SH-WFS is implemented by adding time-domain low-coherence reflectometry gating to an SH-WFS configuration. The depth resolution is determined by the operational depth selection of the coherence gate, much narrower than the depth range of the SH-WFS. Five distinctive wavefronts are measured from five layers of a multiple-layer target. This paves the way toward depth-resolved wavefront sensing, which can significantly improve adaptive optics closed loops applied to microscopy and imaging of the retina. © 2012 Optical Society of America

OCIS codes: 170.4470, 170.4500, 170.3890, 110.1080, 180.0180.

Shack–Hartmann wavefront sensors (SH-WFSs) [1] have been used extensively to provide direct wavefront sensing in close-loop adaptive optics (AO)–assisted imaging techniques [2]. Current SH-WFSs exhibit a large depth range and therefore cannot measure depth-resolved wavefronts. For the same reason, they are vulnerable to stray reflections from the imaging system and the targets. Direct wavefront sensing was deemed unsuitable for microscopy because of the lack of a single point-like reference source [3,4]. In addition, multiple facets of multielements in the microscope objective and multiple reflections from the microscope slides produce strong stray light onto the camera. Such stray reflections create additional spots to the useful spot pattern that confuse slope calculations. There is no simple way to distinguish such spots from the spots that result from the sample. For indirect wavefront sensing, algorithms to maximize sharpness metrics, such as simulated annealing [5] and genetic algorithms [6] have been devised to infer the correction required; however, these usually require several minutes for each point to find the optimum correction [7,8]. Principles of low-coherence interferometry (LCI) have been added to a virtual SH-WFS to narrow its depth range [9,10]. To this goal, a virtual lenslet algorithm was applied to three-dimensional (3D) data collected by an LCI from backscattered light. Similar to an indirect WFS, this numeric coherence gate (CG) method involves a large quantity of computations, which demand long processing time.

In this Letter, we present results using a different approach, where coherence gating was applied directly onto the beams produced by a physical lenslet array (LA). This method has the advantage of much higher speed and can be developed to perform dynamic measurements, as required for fast moving targets in microscopy or for human retinas. In a previous report [11], it was demonstrated that the principle of an SH-WFS is compatible with two formats of implementing a CG, operating in time domain using a broadband optical source and phase-shifting interferometry (PSI) [12], and operating in spectral domain using narrow-band wavelength-scanning interferometry. For this demonstration, we

chose the time-domain approach, because it is more intuitive, providing *en-face* images of SH spots directly. Here, to the best of our knowledge, we demonstrate for the first time the capability of a CG/SH-WFS to measure depth-resolved wavefronts from multiple layer targets in real time, in the presence of strong stray reflections.

The experimental setup of the CG/SH-WFS is illustrated in Fig. 1. A superluminescent diode (SLD), with a central wavelength of 850 nm and an FWHM bandwidth of 20 nm is used as the optical source, determining an axial CG of 16 μm in air. A beam of 10 mm diameter is launched from the SLD by a collimating lens, CL, onto a beam splitter, BS1. Light is divided into an object beam and a reference beam, which are focused by two achromatic doublets, L1 and L2, of focal length 30 mm onto the object, Obj, and onto a reference mirror, RM, respectively. The Obj is mounted on an object translation stage, OTS. The RM is mounted on a Piezo-actuator, PZT, which is driven by a generator, G, to introduce phase modulation. The three elements, L2, RM, and PZT, are mounted

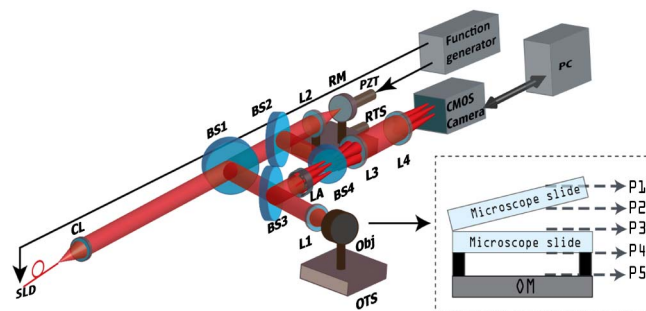


Fig. 1. (Color online) CG/SH-WFS setup. SLD, superluminescent diode; CL, collimating lens; BS1, BS2, BS3, BS4, four plate beamsplitters; RM, reference mirror; Obj, object, made of two nonparallel microscope slides of 1.4 mm thickness mounted in front of a mirror, OM, as shown in the inset; PZT, Piezo-actuator; RTS and OTS, reference and object translation stage, respectively (moving axially); L1, L2, L3, L4, achromatic doublets; LA, lenslet array; P1, P2, P3, P4, and P5 in the inset, the five planes in the Obj where wavefronts originate from.

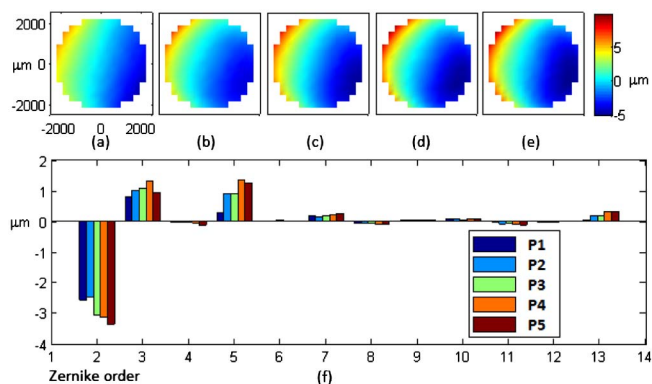


Fig. 3. (Color online) Reconstructed wavefronts from all five layers of the object, (a), (b), (c), (d), and (e), are the wavefronts measured from P1, P2, P3, P4, and P5, respectively; (f) displays the first 13 Zernike coefficients for all measurements.

important are the second, the third, and the fifth coefficients, which are responsible for tilt along x direction, tilt along y direction, and defocus, respectively.

The image Fig. 3(a) was recorded at the axial location where the CG coincides with the focus. When moving the Obj toward BS3 to obtain $OPD = 0$ for the rest of the planes, the focus position moves away from BS3, whereas the CG moves toward BS3, that is, the focus and the CG translate in opposite directions. Therefore, in the process of regaining the $OPD = 0$ at each interface, the axial movement of the whole Obj leads to a mismatch between the axial position of the plane selected by the CG/SH-WFS and the position where the focus should be. This means that only Fig. 3(a) was acquired without sample-induced defocus aberration. In all other images, Figs. 3(b), 3(c), 3(d), and 3(e), the CG and the focus differ, with the focus moved away from BS3. The fifth Zernike coefficients in Fig. 3(f) show the smallest value for P1, where the CG was superposed on the focus, whereas larger values are obtained for the P2 and P3 and even larger for the P4 and P5. Their comparative values are in agreement with the expectations, because the mismatch between the CG and the focus increases from P2 to P5. Because of the similar differences between the focus position and the CG position for the P2 and P3, similar results were obtained for the fifth coefficient. For the same reason, the values of the fifth coefficient for the P4 and P5 are also similar. The results in Fig. 3 also show that aberrations of tilts in the x direction (the second Zernike coefficient) are larger than those in the y direction (the third Zernike coefficient) because of the deliberate tilting of the top slide in the Obj when it was

assembled. These results confirm that measurements of depth-resolved wavefront aberrations are possible from different layers in depth in the same object.

In summary, real-time operation of a CG/SH-WFS setup is demonstrated, capable of producing similar spot patterns as a conventional SH-WFS, from a five-layer target. SH spots from each layer are selected in depth in the presence of stray reflections from the other layers, including strong reflections from one of the layers, a mirror. Depth-resolved wavefront measurements and analysis are demonstrated, from each of the five layers based on each set of SH spots separated by the CG. For the example of the object used, a conventional SH-WFS could not deliver aberration information except from the layer providing strong spots (i.e., the mirror), as too many sets of spots of similar intensity were present in the image. These results are relevant for developing WFSs to be applied to AO microscopy of thick samples. The capability of depth-resolved aberration measurement may lead to new approaches of wavefront correction in AO-assisted ophthalmology. Further work is required to validate the method in imaging scattering targets.

The authors acknowledge support from the ERCCO-GATIMABIO, grant 249889.

References

1. R. K. Tyson and M. Dekker, *Adaptive Optics Engineering Handbook* (Marcel Dekker, 1999).
2. A. Roorda, F. Romero-Borja, I. I. I. W. Donnelly, H. Queener, T. Hebert, and M. Campbell, *Opt. Express* **10**, 405 (2002).
3. M. J. Booth, *Phil. Trans. R. Soc. A* **365**, 2829 (2007).
4. M. J. Booth, M. A. A. Neil, R. Juskaitis, and T. Wilson, *Proc. Natl. Acad. Sci. USA*, **99**, 5788 (2002).
5. M. Nieto-Vesperinas, R. Navarro, and F. J. Fuentes, *J. Opt. Soc. Am. A* **5**, 30 (1988).
6. Y. Yasuno, T. F. Wiesendanger, A. K. Ruprecht, S. Makita, T. Yatagai, and H. J. Tiziani, *Opt. Commun.* **232**, 91 (2004).
7. J. R. Fienup and J. J. Miller, *J. Opt. Soc. Am. A* **20**, 609 (2003).
8. P. Marsh, D. Burns, and J. Girkin, *Opt. Express* **11**, 1123 (2003).
9. M. Feierabend, M. Rückel, and W. Denk, *Opt. Lett.* **29**, 2255 (2004).
10. M. Rueckel, J. A. Mack-Bucher, and W. Denk, *Proc. Natl. Acad. Sci. USA* **103**, 17137 (2006).
11. S. Tuohy and A. G. Podoleanu, *Opt. Express* **18**, 3458 (2010).
12. A. Dubois, G. Moneron, and C. Boccara, *Opt. Commun.* **266**, 738 (2006).
13. L. Vabre, A. Dubois, and A. C. Boccara, *Opt. Lett.* **27**, 530 (2002).
14. N. A. Roddier, *Opt. Eng.* **29**, 1174 (1990).